Nanoscale

PAPER

View Article Online
View Journal | View Issue

Cite this: *Nanoscale*, 2014, **6**, 7461

Facile synthesis of intense green light emitting $LiGdF_4$:Yb,Er-based upconversion bipyramidal nanocrystals and their polymer composites†

Hyejin Na,[a] Jong Seok Jeong,[b] Hye Jung Chang,[c] Hyun You Kim,[de] Kyoungja Woo,[a] Kipil Lim,[a] K. Andre Mkhoyan[b] and Ho Seong Jang‡*[a]

Received 16th February 2014
Accepted 10th April 2014

DOI: 10.1039/c4nr00857j

www.rsc.org/nanoscale

A pathway for achieving intense green light emitting $LiGdF_4$:Yb,Er upconversion nanophosphors (UCNPs) *via* Y^{3+} doping is demonstrated. It was revealed that Y^{3+} doping initiated the formation of a tetragonal phase and affected the particle size. Single tetragonal-phase $LiGd_{0.4}Y_{0.4}F_4$:Yb(18%),Er(2%) ($LGY_{0.4}F$:Yb,Er) UCNPs exhibited strong upconversion (UC) green luminescence and tetragonal bipyramidal morphologies. They showed 1325 and 325-fold higher photoluminescence intensity than the 0 and 80 mol% Y^{3+}-doped $LiGdF_4$:Yb,Er UCNPs, respectively. Additionally the particle size (edge length) of $LiGdF_4$:Yb,Er-based upconversion tetragonal bipyramids (UCTBs) was controlled from 60.5 nm to an ultrasmall size of 9.3 nm with varying Y^{3+} doping concentration. In an $LGY_{0.4}F$:Yb,Er UCTB, uniform distribution of all constituent elements was directly confirmed by using high-angle annular dark-field scanning transmission electron microscopy and energy-filtered transmission electron microscopy (EFTEM) image analyses. In particular, existence of activator Er^{3+} ions with extremely small quantity was clearly seen over a particle on the EFTEM image. Moreover, the $LGY_{0.4}F$:Yb,Er UCTBs were successfully incorporated into the polydimethylsiloxane (PDMS) polymer and the highly transparent UCTB–PDMS composites showed bright green light under the excitation of 980 nm infrared light.

1. Introduction

Lanthanide doping into inorganic crystals imparts these materials with new functionalities such as upconversion (UC),[1–3] downconversion/downshifting,[4–7] dual-mode luminescence,[8–10] enhanced computed tomography (CT) contrast[11] and magnetism.[12,13] In particular, lanthanide ion-doped (Ln^{3+}-doped) upconversion nanophosphors (UCNPs) have been in the spotlight due to their excellent chemical and optical properties. The UCNPs have many advantages over conventional fluorescent organic dyes and quantum dots, such as high photostability (without photobleaching), long life time (from μs to ms) due to the luminescence attributed to parity-forbidden f–f transition, large anti-Stokes shifts, non-toxicity (no Cd or Pb), and a lack of photoblinking.[14] Moreover, the UCNPs exhibit an infrared (IR) to visible light conversion efficiency an order of magnitude higher than the two-photon absorption process. This high conversion efficiency of the UCNPs is due to the existence of a real, intermediate energy level between the ground and excited states.[14,15] Given this high UC efficiency, commercially available, inexpensive continuous-wave diode lasers can be used as an excitation light source. Recently, sub-10 nm, ultrasmall UCNPs were successfully synthesized with excellent luminescent properties that could allow further bioimaging applications.[16,17]

To date, Ln^{3+}-doped fluoride-based UCNPs have been extensively studied, because fluoride materials have low phonon energies and show high optical transparency in the visible region due to their large band-gap energy.[18,19] In particular, $NaLnF_4$ (Ln = Gd, La, Lu, and Y)-based UCNPs have attracted great attention.[17,20–25] For example, β-$NaYF_4$ is known as the most efficient host material for blue and green upconversion luminescence.[26] On the other hand, $LiGdF_4$ is an outstanding host for downconversion luminescence with a visible quantum efficiency approaching 190%.[27] However, although $LiYF_4$:Yb,Tm/Er and $LiYF_4$:Er UCNPs have been reported,[28–31] few reports describe $LiGdF_4$-based UCNPs possibly

[a]*Molecular Recognition Research Center, Korea Institute of Science and Technology, Hwarangno 14-gil 5, Seongbuk-gu, Seoul 136-791, Republic of Korea. E-mail: msekorea@kist.re.kr; Fax: +82-2-958-5451; Tel: +82-2-958-5263*

[b]*Department of Chemical Engineering and Materials Science, University of Minnesota, 421 Washington Avenue SE, Minneapolis, MN 55455, USA*

[c]*Advanced Analysis Center, Korea Institute of Science and Technology, Hwarangno 14-gil 5, Seongbuk-gu, Seoul 136-791, Republic of Korea*

[d]*Center for Functional Nanomaterials, Brookhaven National Laboratory, Upton, New York 11973, USA*

[e]*Department of Nanomaterials Engineering, Chungnam National University, 99 Daehak-ro, Yuseong-gu, Daejeon 305-764, Republic of Korea*

† Electronic supplementary information (ESI) available. See DOI: 10.1039/c4nr00857j

‡ Present address: Center for Materials Architecturing, Korea Institute of Science and Technology, Hwarangno 14-gil 5, Seongbuk-gu, Seoul 136-791, Republic of Korea.

due to the difficulty in synthesizing $LiGdF_4$ nanocrystals with a single tetragonal phase.[32] Because lanthanide doping simultaneously affects both the size and phase of the UCNPs,[33] we used Y doping as the synthesis pathway for the fabrication of single-phase $LiGdF_4$ UCNPs. In this article, we report on the facile synthesis of highly bright Y^{3+}-doped $LiGdF_4$:Yb,Er UCNPs with a single tetragonal phase. The $Li(Gd,Y)F_4$:Yb,Er showed intense green UC luminescence with higher efficiency than β-$NaYF_4$:Yb,Er UCNPs at 150 W cm^{-2} power density and a tunable size from several tens of nanometers to sub-10 nm *via* Y^{3+} doping. In addition, the applicability of the $Li(Gd,Y)F_4$:Yb,Er UCNPs to transparent display devices was examined through fabrication of transparent polymer composites.

On the other hand, one must establish a compositional map of these UCNPs and the locations of the activator Ln^{3+} ions within the particles because the luminescence of the UCNPs is strongly affected by surface defects.[34,35] Although the dopant distribution in the Ln^{3+}-doped $NaGdF_4$ has been analyzed *via* synchrotron X-ray photoelectron spectroscopy (XPS), determining the precise elemental distribution at the single-nanoparticle level remains difficult because the XPS technique is an ensemble measurement.[36] Thus, transmission electron microscopy (TEM) combined with energy dispersive X-ray spectroscopy (EDS) and electron energy-loss spectroscopy (EELS) analysis is necessary to identify the compositional distributions within a nanoparticle. Here, for the first time, we successfully synthesized highly bright, single-phase $LiGdF_4$-based UC tetragonal bipyramids (UCTBs) *via* Y doping. We also provide direct identification of the elemental distribution of each constituent in the UCTBs by applying energy-filtered TEM (EFTEM) and high-angle annular dark-field scanning transmission electron microscopy (HAADF STEM).

2. Experimental

2.1. Materials

$LiOH\cdot H_2O$ (99.995%), $GdCl_3\cdot 6H_2O$ (99%), $YCl_3\cdot 6H_2O$ (99.99%), $YbCl_3\cdot 6H_2O$ (99.9%), $ErCl_3\cdot 6H_2O$ (99.9%), NH_4F (99.99+%), oleic acid (OA, technical grade 90%), and 1-octadecene (ODE, technical grade 90%) were purchased from Aldrich and they were used without further purification. Sodium oleate (>97%) was obtained from TCI.

2.2. Synthesis of the $Li(Gd,Y)F_4$:Yb,Er upconversion nanophosphors

First, the lanthanide oleates [$Ln(oleate)_3$, Ln = Gd, Y, Yb, and Er] were prepared by adopting the synthesis reported by Hyeon's group.[37] Then, 1 mmol of $Ln(oleate)_3$ complexes, in which the quantities of Yb and Er were fixed at 0.18 and 0.02 mmol, respectively, were loaded into a three-necked flask containing a solvent mixture of 10.5 ml OA and 10.5 ml ODE. The mixture was heated to 150 °C for 40 min to yield a transparent solution. After the reaction mixture cooled to 50 °C, a methanol (MeOH) solution (10 ml) containing $LiOH\cdot H_2O$ (2.5 mmol) and NH_4F (4 mmol) was added to the reaction flask and then stirred for 40 min. After the MeOH was removed, the solution was heated to 320 °C for 90 min under an Ar atmosphere. The as-synthesized nanophosphors were washed several times with ethanol and dispersed in chloroform.

2.3. Preparation of the UCTB–PDMS composites

To prepare the UCTB–polydimethylsiloxane (PDMS) composites, 0.4 ml of UCTB solution (approximately 1 wt%) was thoroughly mixed with 10 ml of SYLGARD silicone elastomer 184 followed by the addition of a curing agent (1 ml). Finally, the UCTB–PDMS composites (approximately 0.04 wt% UCTB) were aged overnight and then heat-treated at 80 °C for 1 h.

2.4. Characterization

The absorption and transmittance spectra were recorded using a Perkin-Elmer Lambda25 UV/VIS spectrophotometer. The absorption spectrum of the UCNP chloroform solution (~1 wt %) in a quartz cuvette (1 cm × 1 cm, Hellma QS cell) was recorded under the conditions of 240 nm min^{-1} of scan speed and 1 nm of slit width. The crystal structures of the as-synthesized nanophosphors were determined using a Bruker D8 ADVANCE diffractometer with Cu K_α radiation at 40 kV and 40 mA. The photoluminescence (PL) spectra were collected using a Hitachi F-7000 spectrophotometer. The scanning electron microscopy (SEM) and TEM images were obtained on an FEI Nova nanoSEM operating at 10 kV and a Tecnai G2 F20 operating at 200 kV, respectively. The EFTEM images were obtained on an FEI Titan 80/300 operating at 300 kV equipped with a GIF Quantum®ERS (Gatan, Inc., USA). The high-resolution STEM (HR-STEM) images were obtained using an FEI Tecnai G2 F30 S-TEM operating at 300 kV.

2.5. Density functional theory (DFT) calculation

We performed spin-polarized density functional theory (DFT) calculation on a plane-wave basis with the Vienna *Ab initio* Simulation Package (VASP) code[38] and the Perdew–Burke–Ernzerhof (PBE) sol[39] GGA functional. Valence electrons were described by plane waves up to an energy cutoff of 400 eV and the core electrons were described within the projector augmented wave framework.[40] We used a 6 × 6 × 3 *k*-points grid sampling of the Brillouin zone for unit cell calculations. Final convergence criteria for the electronic wave function and geometry were 10^{-4} eV and 0.01 eV $Å^{-1}$, respectively. The Gaussian smearing method with a width of 0.05 eV was used to improve convergence with respect to states near the Fermi level.

3. Results and discussion

All UCNP solutions, which are highly transparent, exhibited green luminescence under IR illumination (Fig. S1†). Fig. 1a presents the PL spectra of the $Li(Gd,Y)F_4$:Yb,Er UCNPs under 980 nm IR excitation (the Yb and Er concentrations were 18 and 2 mol%, respectively). The PL peaks are ascribed to the 4f–4f electronic transitions of the Er^{3+} ions *via* a $Yb^{3+} \rightarrow Er^{3+}$ energy transfer following IR light absorption by the Yb^{3+} which has an absorption band at approximately 960 nm (Fig. S2†). The emission peaks in the green and red spectral regions result

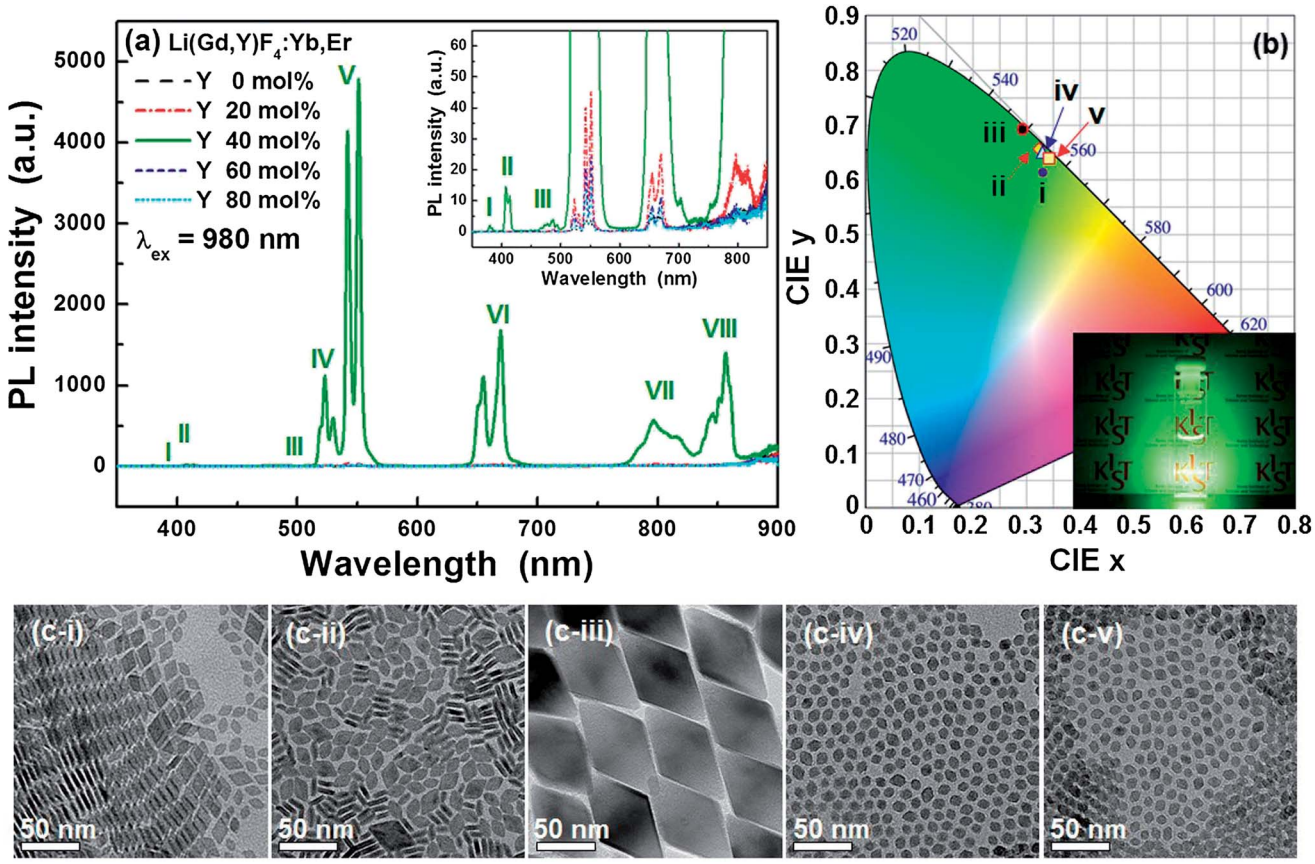

Fig. 1 (a) PL spectra, (b) CIE color coordinates, and (c) TEM images of Li(Gd,Y)F_4:Yb,Er UCNPs. [i: $Y = 0$ mol%, ii: $Y = 20$ mol%, iii: $Y = 40$ mol%, iv: $Y = 60$ mol%, and v: $Y = 80$ mol%]. The inset in (a) shows magnified PL spectra of the low PL intensity region. The inset in (b) shows luminescent $LGY_{0.4}F$:Yb,Er UCNP solutions (~1 wt%) under the irradiation of 980 nm IR diode laser. [I: $^4G_{11/2} \rightarrow {}^4I_{15/2}$, II: $^2H_{9/2} \rightarrow {}^4I_{15/2}$, III: $^4F_{7/2} \rightarrow {}^4I_{15/2}$, IV: $^2H_{11/2} \rightarrow {}^4I_{15/2}$, V: $^4S_{3/2} \rightarrow {}^4I_{15/2}$, VI: $^4F_{9/2} \rightarrow {}^4I_{15/2}$, VII: $^4I_{9/2} \rightarrow {}^4I_{15/2}$, and VIII: $^4S_{3/2} \rightarrow {}^4I_{13/2}$].

from the two-photon upconversion process, as evidenced by the light power-dependent PL intensity (see Fig. S3†). As the Y^{3+} concentration increased to 40 mol% in the host lattice, the PL intensity increased. At higher Y^{3+} concentrations, however, the PL intensity decreased significantly. For example, 40 mol% Y^{3+}-doped $LiGdF_4$:Yb,Er ($LGY_{0.4}F$:Yb,Er) exhibited an approximately 1325 and 325-fold higher PL intensity than the 0 and 80 mol% Y^{3+}-doped $LiGdF_4$:Yb,Er UCNPs, respectively. Given the strong PL intensity ascribed to the $^4S_{3/2} \rightarrow {}^4I_{15/2}$ transition, which peaks at 550 nm, the $LGY_{0.4}F$:Yb,Er UCNPs emit a bright green light, as depicted in Fig. 1b inset. Previously, Chen *et al.* obtained the quantum yield (QY) of $LiYF_4$:Er UCNPs by comparing with β-$NaYF_4$:Yb,Er UCNPs.[30] When the PL intensity of the $LGY_{0.4}F$:Yb,Er UCNPs was compared with that of β-$NaYF_4$:Yb,Er UCNPs, the $LGY_{0.4}F$:Yb,Er showed higher PL intensity (Fig. S5†). Its QY was calculated to be 0.16% by using the QY (0.1%) of β-$NaYF_4$:Yb,Er with 30 nm size.[41] Although the relative QY of the $LGY_{0.4}F$:Yb,Er UCNPs was obtained in the current study, absolute QY of the $LGY_{0.4}F$:Yb,Er UCNPs will be further studied by using an integrating sphere. When we calculated the intensity ratio of green to red emission ($R_{g/r}$) of the Li(Gd,Y)F_4:Yb,Er UCNPs, the $R_{g/r}$ value increased with increasing Y^{3+} concentration under the conditions of 0 and 20 mol% Y^{3+} doping. In that case, the particle size increased with increasing Y^{3+} concentration. On the other hand, the $R_{g/r}$ value decreased when the particle size decreased with increasing Y^{3+} concentration (Y^{3+} concentration = 40, 60, and 80 mol%). As shown in Fig. S6,† $LGY_{0.4}F$:Yb,Er showed the highest $R_{g/r}$ value of 2.85. As a consequence, the $R_{g/r}$ value was dependent on the particle size and it decreased with decreasing particle size. When the particle size decreases, quenching of UC luminescence induced by surface defects and ligands becomes more important and it modifies the relative population among various excited states through phonon-assisted nonradiative relaxations.[42,43] However, although the edge size of the 20 mol% Y^{3+}-doped Li(Gd,Y)F_4:Yb,Er was larger than that of 60 mol% Y^{3+}-doped Li(Gd,Y)$_4$:Yb,Er, its $R_{g/r}$ value was smaller than that of the 60 mol% Y^{3+}-doped Li(Gd,Y)F_4:Yb,Er due to the different crystal structure (see Fig. S6†). The Commission Internationale de l'Eclairage (CIE) color coordinates (x, y) of the $LGY_{0.4}F$:Yb,Er UCNPs are (0.2929, 0.6917). The $LGY_{0.4}F$:Yb,Er UCNPs exhibit a very high color purity of 98.9%, which approaches that of monochromatic light due to the sharp emission peak and high green-to-red ratio in the PL intensity.

As indicated in Fig. 1c, the $LGY_{0.4}F$:Yb,Er UCNPs are much larger than the other Li(Gd,Y)F_4:Yb,Er UCNPs. In addition, the X-ray diffraction (XRD) patterns presented in Fig. S7† reveal the formation of an orthorhombic GdF_3 phase under doping

conditions between 0 and 20 mol% Y^{3+}. The crystal structures were also verified from the UCNP lattice spacings measured *via* high-resolution TEM (HR-TEM) (Fig. S8†). A tetragonal $LiGdF_4$ phase (the $LiYF_4$ phase for 80 mol% Y^{3+} doping) was formed under doping conditions between 40 and 80 mol% Y^{3+}. It was reported that a single $LiGdF_4$ tetragonal phase is hardly synthesized and instead, GdF_3 orthorhombic phase is apt to be formed.[32] However, as the Gd^{3+} ions were replaced by Y^{3+} ions (>20 mol%), a tetragonal phase was formed without changing the reaction temperature and/or time, which may be attributed to a decrease in the energetic barrier for the formation of a $LiGdF_4$ phase due to lanthanide doping.[33] Large size and formation of a single tetragonal phase may be attributed to strong UC luminescence of $LGY_{0.4}F$:Yb,Er UCNPs. It is believed that the size effect is more dominant on the luminescence than the phase effect, judging from similar brightness of small UCNPs corresponding to Fig. 1c-i, ii, iv, and v, as shown in Fig. 1 and S1b.† However, further study is necessary to reveal the exact origin of strong UC luminescence from $LGY_{0.4}F$:Yb,Er UCNPs. It is noted that the particle size could be controlled *via* Ln^{3+} ion doping for the case of the $LiGdF_4$ tetragonal phase, whereas it was hardly controlled for the GdF_3 orthorhombic phase. Thus, we can achieve intense UC luminescence by simply controlling the particle size when we synthesize a single tetragonal $LiGdF_4$ phase. In addition, morphologies of the $Li(Gd,Y)F_4$:Yb,Er UCNPs are affected by their phases. Minute differences may be noted in the TEM images in Fig. 1c. The UCNP morphologies in Fig. 1c-i and ii exhibit rhombic plate-like shapes, while the plate shape was not observed in Fig. 1c-iii to v. The particle shapes in Fig. 1c-iv and c-v appear octahedral or truncated octahedral. This morphological difference is believed to result from their different crystal structures. The rhombic plates depicted in Fig. 1c-i have edge lengths of 12.1 ± 1.0 nm and thicknesses of 4.0 ± 0.5 nm. The nanoplates are easily aligned into two-dimensional aggregates as shown in Fig. 1c-i and S9† because this alignment minimizes the free energy by hydrophobic interactions of the surface ligands of the nanoplates at their largest faces.[44] As the quantity of Y^{3+} ions increased in the host lattice, the particle size decreased from 60.5 nm (edge length) for the 40 mol% Y^{3+} doping to 9.3 nm (edge length) for the 80 mol% Y^{3+} doping, which resulted in weak PL intensities for the $Li(Gd,Y)F_4$:Yb,Er. As observed in Fig. 1c-iv and c-v, the small $Li(Gd,Y)F_4$:Yb,Er UCNPs appear somewhat spherical with slight faceting, while the large $LGY_{0.4}F$:Yb,Er UCNPs exhibit sharp facets.

We studied the trend in the change of the particle sizes of the $Li(Gd,Y)F_4$:Yb,Er UCNPs with tetragonal structure as a function of Y^{3+} concentration from 40 mol% to 80 mol%. In the high concentration regime, 60 and 80 mol% Y^{3+}, the difference in the particle size was marginally small (see Table S1† and Fig. S10†). However, there was significant increase in the particle size between 60 and 40 mol% Y^{3+}-doped $Li(Gd,Y)F_4$:Yb,Er UCNPs; the $LGY_{0.4}F$:Yb,Er UCNPs were approximately 6 times larger than the 60 mol% Y^{3+}-doped $Li(Gd,Y)F_4$:Yb,Er UCNPs. Previously, Wang *et al.* studied the size change of $NaYF_4$:Yb,Er UCNPs by Gd^{3+} doping by using density functional theory (DFT) calculation.[33] They found that the Gd^{3+} ions donate more electron density to adjacent F^- ions than Y^{3+} ions do leading to the increased electron polarization between cations and F^- ions. Increased electrostatic repulsive force between the electron rich F^- ions at the surface layer of $NaYF_4$ and F^- ions in the solution can substantially slow down the diffusion of F^- ions from solution to the nanocrystal surface. They associated this with the reduced nanocrystal size.[33] In contrast to the case of $NaYF_4$, the Bader charge analysis[45,46] on a unit-cell of $LiYF_4$, $LiGdF_4$, and $Li(Gd_{0.5},Y_{0.5})F_4$ ($LiGdYF_4$) shows that there is no significant charge redistribution upon Y^{3+} doping in the bulk level as shown in Table S2.† It may attribute to experimentally observed small change in the size of the nanocrystals for 60 and 80 mol% Y^{3+} doping. However, in the case of similar concentrations of Y^{3+} to Gd^{3+}, upon surface formation, some of the surface-exposed F^- ions adjacent to Y^{3+} dopants of the most stable $LiGdYF_4(101)$ surface, which is experimentally and theoretically confirmed (see below), were less-negatively charged compared to the F^- ions in a bulk phase ($\Delta e = 0.06$). According to the discussion in ref. 33, we postulate that these less-negatively charged F^- ions will reduce the electrostatic repulsive force upon the approach of F^- ions in solution to the $LiGdYF_4(101)$ surface and thus can accelerate the formation of $LiGdYF_4$ with large size.

Previous reports indicate that $LiYF_4$-based nanocrystals are plate shaped.[28,32] Although a TEM image of the $LGY_{0.4}F$:Yb,Er observed along a particular crystallographic orientation (Fig. 1c-iii) demonstrates a plate-like shape, the actual morphology of the $LGY_{0.4}F$:Yb,Er is octahedral as indicated in Fig. 2. Fig. 2a presents a TEM image of the $LGY_{0.4}F$:Yb,Er particles that were not aligned parallel to the TEM gird. No plate-shaped particles were observed in our TEM images of the $Li(Gd,Y)F_4$:Yb,Er UCNPs for 40, 60, and 80 mol% Y^{3+} doping. As demonstrated in the TEM images in Fig. 2a, the central portions of the $LGY_{0.4}F$:Yb,Er UCNPs are much darker than their edges (*vice versa* in the HAADF STEM images, Fig. S11†). This severe contrast in the UCNPs indicates that the UCNPs are thicker in their centers than at the edges. The STEM and SEM studies also revealed that $LGY_{0.4}F$:Yb,Er exhibits a tetragonal bipyramidal morphology (Fig. S11 and S12†). The HR-TEM and HAADF HR-STEM analyses of the $LGY_{0.4}F$:Yb,Er UCTBs shown in Fig. 2 proved that the particles were bound by {101} planes. The angles between two adjacent planes were measured to be 50.7 and 129.3° which are in agreement with the angles between the (101) and $(10\bar{1})$ planes of tetragonal $LiGdF_4$. The fast Fourier transform (FFT) pattern presented in the inset of Fig. 2b can be indexed to be the zone axis along the [010] direction of the tetragonal $LiGdF_4$ structure. The results indicate that $LGY_{0.4}F$:Yb,Er UCTBs have a single crystalline phase with high crystallinity. To investigate the origin of the formation of the tetragonal bipyramidal morphology, the surface energies of the low-index planes of $Li(Gd,Y)F_4$ – (100), (101) and (111) – were calculated using density functional theory. The unit cell of $LiGdF_4$ was initially optimized and two ions of Gd^{3+} were substituted with Y^{3+} ions. The unit cell of $Li(Gd_{0.5},Y_{0.5})F_4$ with the most stable configuration of Gd^{3+} and Y^{3+} ions is presented in Fig. 3a. The morphology of each plane and their surface energies are presented in Fig. 3b–d and Table 1, respectively. The calculations confirm that the (101) surface is thermodynamically favored. The $LGY_{0.4}F$:Yb,Er UCTBs are faceted by eight equivalent {101} planes in a tetragonal structure, which induces a tetragonal

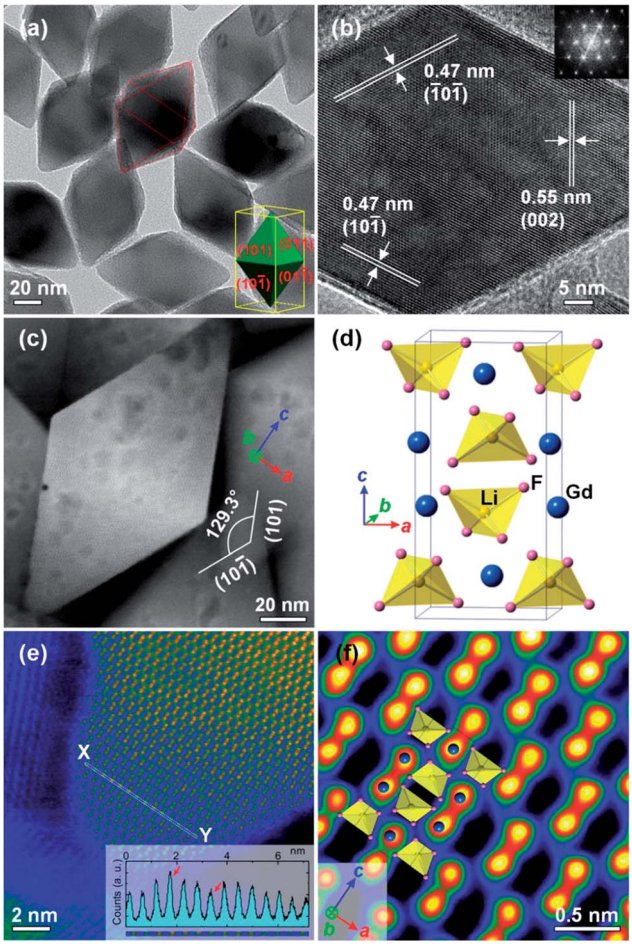

Fig. 2 (a) Bright-field TEM, (b) HR-TEM, and (c) HAADF STEM images, (d) perspective view of $LGY_{0.4}F$:Yb,Er unit cell structure, (e) HAADF HR-STEM and (f) filtered HAADF HR-STEM images of $LGY_{0.4}F$:Yb,Er UCTBs. The inset in (a) shows a schematic diagram of the crystal morphology and the inset of (b) indicates the FFT diffractogram for the HR-TEM image. The inset in (e) indicates the *Z*-contrast intensity profile across line *XY*. The [010]-projection of the unit cell is superimposed in (f) filtered HAADF HR-STEM image of $LGY_{0.4}F$:Yb,Er UCTBs.

Table 1 DFT calculated surface energies of (100), (101), and (111) planes of the $Li(Gd_{0.5}Y_{0.5})F_4$ host crystal

Surface index	(100)	(101)	(111)
Surface energy (eV $Å^{-2}$)	0.418	0.051	0.098
Surface energy (J m^{-2})	6.67	0.82	1.57

bipyramidal morphology due to a longer lattice parameter along the *c*-axis. The lattice parameters, $a = b = 5.177$ Å and $c = 10.773$ Å, were calculated from the high resolution XRD pattern. All facets are atomically flat, and the two apices along the *c*-axis are blunt (Fig. S13†). The tips are blunt in the cross-sectional region of the approximately 20 × 20 unit cell $(uc)^2$ in the *ab* plane (Fig. S13†).

The *Z*-contrast of the atomic columns was examined in the HAADF STEM images (Fig. 2e). The potential contrast variation by electron beam damage, which was observed in highly exposed areas (Fig. 2c and S14, S15†), can largely be prevented by acquiring fresh STEM images. The intensity profile across *XY* indicates considerable variation: a higher intensity can support the existence of dopants such as Er and Yb in the Gd sites, and a lower intensity can indicate *Y* in Gd sites as designated by the arrows (see also Fig. S14†). The lanthanide elements are clearly observed in the low-pass filtered HAADF HR-STEM image (Fig. 2f), and their arrangement is consistent with a projection of the $LiGdF_4$ unit cell in the [010] direction. The $LiGdF_4$ has a scheelite structure ($I4_1/a$, $Z = 4$), and the Li^+ and Gd^{3+} ions are four-fold and eight-fold coordinated by the F^- ions, respectively (Fig. 2d).[47,48] It should be noted that the Li and F atoms are not visible in the HAADF STEM image in Fig. 2f because they are very light in comparison with the Y^{3+} and Ln^{3+} ions.

The elemental distribution within a nanoparticle was examined using an EELS-based EFTEM technique. For the materials containing Li, such as our $LGY_{0.4}F$:Yb,Er UCTBs, EELS analysis is a powerful tool because, unlike EDS, it can detect light elements such as Li. Additionally, EFTEM provides rapid elemental mapping for electron-beam-sensitive materials. Fig. 4 presents an elastic TEM image and thickness map of the $LGY_{0.4}F$:Yb,Er

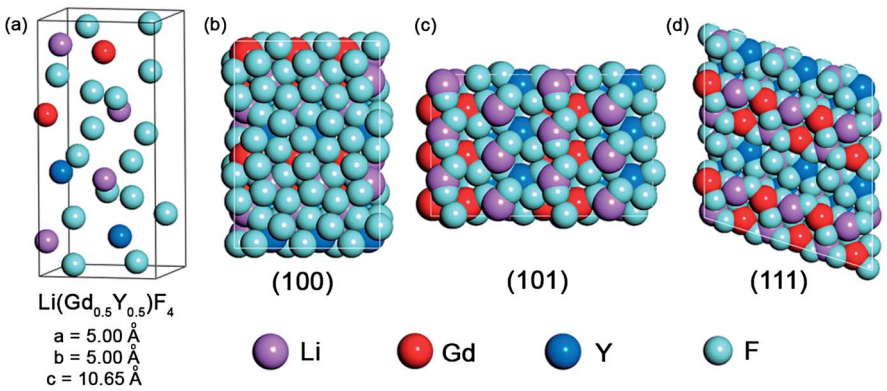

Fig. 3 Morphology of the $Li(Gd_{0.5}Y_{0.5})F_4$ host crystal: (a) a single unit cell, (b) a 3 × 2 × 1 supercell of the (100) plane, (c) a 2 × 3 × 1 supercell of the (101) plane, and (d) a 3 × 2 × 1 supercell of the (111) plane.

UCTBs and the corresponding elemental maps. The core-loss EELS spectra of the Li–K, Gd–$M_{4,5}$, Y–$L_{2,3}$, F–K, Yb–$M_{4,5}$, and Er–$M_{4,5}$ maps obtained from the $LGY_{0.4}F$:Yb,Er UCTBs are presented in Fig. S16.† Acquiring the high energy-loss spectra in TEM (above approximately 1500 eV) is challenging due to the small signal-to-noise ratio. Surprisingly, however, the core-loss edges such as the Gd–$M_{4,5}$ (1185 eV), Er–$M_{4,5}$ (1409 eV), Yb–$M_{4,5}$ (1528 eV) and even the Y–$L_{2,3}$ (2080 eV) edges were successfully acquired with the enhanced signal-to-noise ratio and collection efficiency of the GIF Quantum®ERS (Gatan, Inc., Pleasanton, CA, USA). As a result, EFTEM maps from all elements including lanthanide elements could be successfully obtained as shown in Fig. 4. One thing to note is that the sharp features observed in the image of Fig. 4a are not observed in the Gd, Y, and Yb EFTEM images of Fig. 4c which appear more rounded due to low signal intensity at thin regions such as the apex and the edge of this bipyramidal nanocrystal (see the thickness map of Fig. 4b), particularly for high energy-loss peaks (above 1000 eV). Except for this smoothing effect, however, one can notice that all elements are uniformly distributed over a single UCTB. Even the quantity of the activator Er^{3+} ion is very small and existence of Er^{3+} ions over a particle is clearly seen.

The as-synthesized $LGY_{0.4}F$:Yb,Er UCTBs were highly uniform in size and shape (60.5 ± 1.6 nm × 55.3 ± 1.4 nm), which allows for two-dimensional (2D) ordered arrangement of $LGY_{0.4}F$:Yb,Er UCTBs (Fig. 5a and S11b†). When the size of the UCTBs decreased due to slight increase of Y^{3+} concentration in the host lattice, an even higher ordered 2D superlattice could be obtained (Fig. 5b–d). The $Li(Gd_{0.35}Y_{0.45})F_4$:Yb,Er ($LGY_{0.45}$F:Yb,Er) also exhibits a single tetragonal phase with high crystallinity (Fig. S17†). The slow evaporation of the solvent allows the $LGY_{0.45}F$:Yb,Er UCTBs to assemble into 2D monolayers in which the {101} planes of the UCTBs are parallel to the TEM grid. The spotty selected area electron diffraction (SAED) pattern supports a highly ordered UCTB assembly. The HAADF STEM image of Fig. 5d confirms that the smaller $LGY_{0.45}F$:Yb,Er constituting the 2D superlattice also has a bipyramidal shape. The bright contrast at the apices results from the overlap of apices of adjacent particles.

The feasibility of applying $LGY_{0.4}F$:Yb,Er UCTBs to transparent volumetric three-dimensional (3D) displays was investigated by incorporating UCTBs into a polydimethylsiloxane (PDMS) polymer. Although these UCTBs have an anisotropic morphology and are larger than the previously reported NPs that were successfully incorporated into a PDMS polymer,[33] they were well-dispersed in the PDMS polymer, which allowed for the fabrication of highly transparent UCTB–PDMS composites (Fig. 6). The transmittance of the UCTB–PDMS composites was found to exceed 90% in the visible spectral region (Fig. 6a). As indicated in the photographs of the $LGY_{0.4}F$:Yb,Er UCTB–PDMS bar and disk in Fig. 6c, the luminescence is homogenous, bright green and sufficiently intense to render characters on the

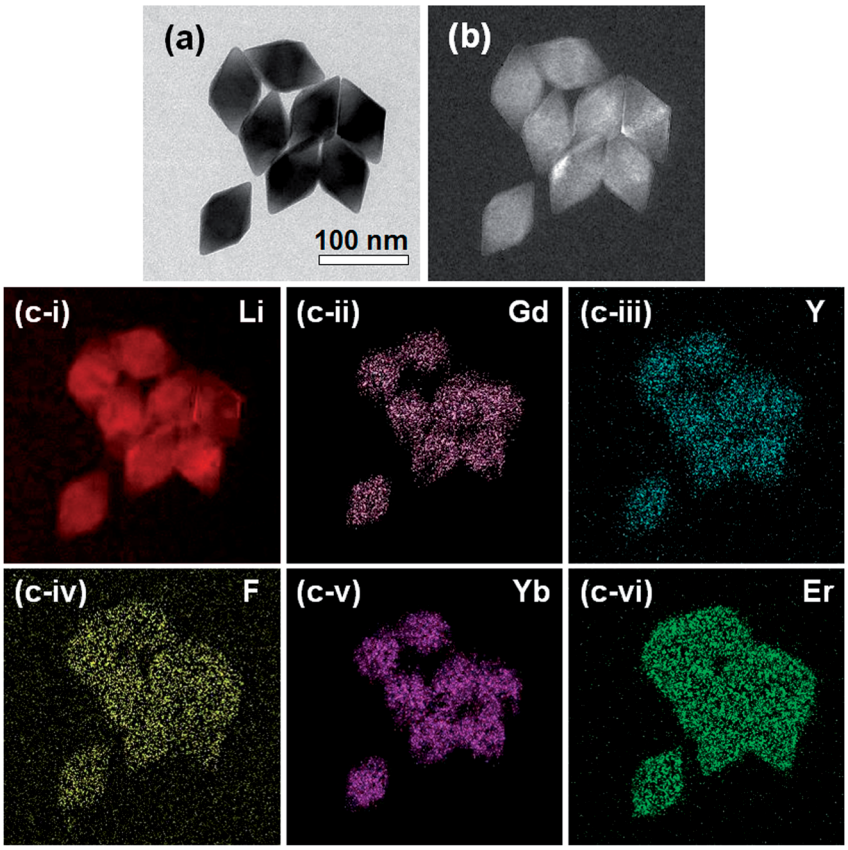

Fig. 4 (a) Elastic TEM image and (b) thickness map of $LGY_{0.4}F$:Yb,Er UCTBs. (c) EFTEM elemental maps for (i) Li, (ii) Gd, (iii) Y, (iv) F, (v) Yb, and (vi) Er are shown.

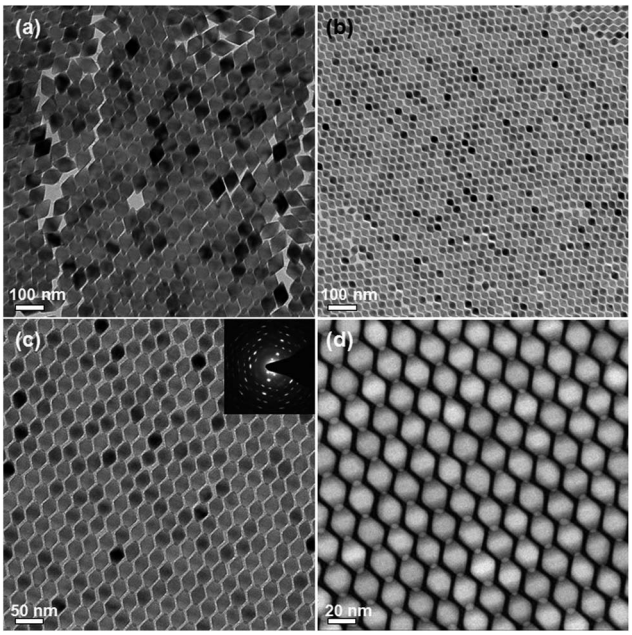

Fig. 5 (a) TEM image of $LGY_{0.4}F$:Yb,Er, (b and c) TEM and (d) STEM images of $LGY_{0.45}F$:Yb,Er UCTBs. The inset in (c) shows a corresponding SAED pattern showing diffraction spots resulting from the superlattice of the $LGY_{0.45}F$:Yb,Er UCTBs.

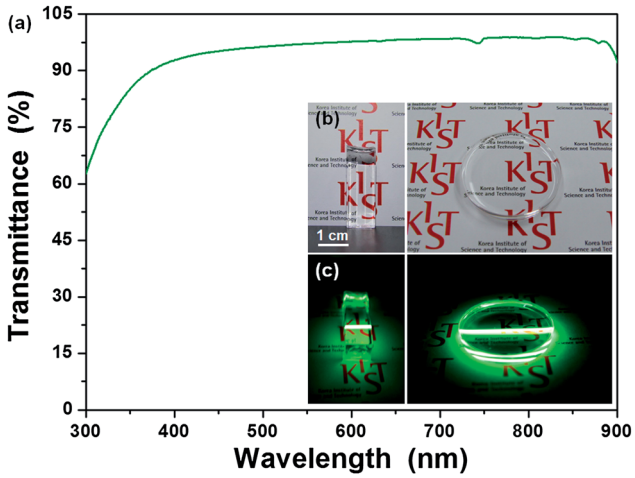

Fig. 6 (a) Transmittance spectrum of $LGY_{0.4}F$:Yb,Er UCTB–PDMS bar and digital camera images of $LGY_{0.4}F$:Yb,Er UCTB–PDMS bar (left) and disk (right) under (b) ambient conditions and (c) IR light irradiation.

background paper legible. The high transparency and brightness of the UCTB–PDMS composites can be attributed to the strong UC luminescence from the $LGY_{0.4}F$:Yb,Er UCTBs which allows small quantities of UCTBs to mix with PDMS. These results also indicate that the UCTBs have potential for applications in volumetric 3D displays.[1,33]

4. Conclusions

In summary, we demonstrated a pathway for achieving intense green light emitting $LiGdF_4$:Yb,Er UCNPs *via* Y^{3+} doping. We found that Y^{3+} doping initiated the formation of a tetragonal phase and affected the particle size. Single tetragonal-phase $Li(Gd,Y)F_4$:Yb,Er UCNPs with Y^{3+} concentrations similar to the Gd^{3+} concentration exhibited intense UC green luminescence and tetragonal bipyramid morphologies. Additionally, sub-10 nm ultrasmall UCTBs could be obtained *via* Y^{3+} doping. Uniform distribution of all constituent elements of $LGY_{0.4}F$:Yb,Er UCTBs was directly seen *via* EFTEM mapping. These $LGY_{0.4}F$:Yb,Er UCTBs were also successfully incorporated into and uniformly distributed throughout PDMS polymer composites. The strong UC luminescence of the $LGY_{0.4}F$:Yb,Er allowed the fabrication of highly transparent and bright green light emitting PDMS composites. These $Li(Gd,Y)F_4$:Yb,Er materials are potentially applicable in transparent volumetric 3D displays.

Acknowledgements

This work was supported in part by the Dream project (2V03410) and Flagship project (2E24572) funded by the Korea Institute of Science and Technology (KIST), the Pioneer Research Center Program through the National Research Foundation of Korea funded by the Ministry of Science, ICT & Future Planning (NRF-2013M3C1A3065040), the MRSEC Program of the National Science Foundation (NSF) under Award number DMR-0819885, and the U.S. Department of Energy, Office of Basic Energy Sciences, under Contract DE-AC02-98CH10886 (H.Y.K.), and parts of this work were carried out in the Characterization Facility, University of Minnesota, which receives partial support from the NSF through the MRSEC program. We thank Seo Kyoung Ryu and Min Kyoung Cho for their technical help for EFTEM analysis (2V02951).

References

1 H. Na, K. Woo, K. Lim and H. S. Jang, *Nanoscale*, 2013, **5**, 4242.
2 Z. Li and Y. Zhang, *Angew. Chem., Int. Ed.*, 2006, **45**, 7732.
3 F. Zhang, Y. Wan, T. Yu, F. Zhang, Y. Shi, S. Xie, Y. Li, L. Xu, B. Tu and D. Zhao, *Angew. Chem., Int. Ed.*, 2007, **46**, 7976.
4 H. S. Jang, H. Yang, S. W. Kim, J. Y. Han, S.-G. Lee and D. Y. Jeon, *Adv. Mater.*, 2008, **20**, 2696.
5 C. Feldmann, T. Justel, C. R. Ronda and D. U. Wiechert, *J. Lumin.*, 2001, **92**, 245.
6 H. S. Jang, H. Y. Kim, Y.-S. Kim, H. M. Lee and D. Y. Jeon, *Opt. Express*, 2012, **20**, 2761.
7 S. Y. Kim, K. Woo, K. Lim, K. Lee and H. S. Jang, *Nanoscale*, 2013, **5**, 9255.
8 H. S. Jang, K. Woo and K. Lim, *Opt. Express*, 2012, **20**, 17107.
9 P. Li, Q. Peng and Y. D. Li, *Adv. Mater.*, 2009, **21**, 1945.
10 Y. Liu, D. Tu, H. Zhu, R. Li, W. Luo and X. Chen, *Adv. Mater.*, 2010, **22**, 3266.
11 Y. Liu, K. Ai, J. Liu, Q. Yuan, Y. He and L. Lu, *Angew. Chem., Int. Ed.*, 2012, **51**, 1437.
12 Y. Liu, D. Wang, J. Shi, Q. Peng and Y. Li, *Angew. Chem., Int. Ed.*, 2013, **52**, 4366.
13 R. Kumar, M. Nyk, T. Y. Ohulchanskyy, C. A. Flask and P. N. Prasad, *Adv. Funct. Mater.*, 2009, **19**, 853.

14 S. Wu, G. Han, D. J. Milliron, S. Aloni, V. Altoe, D. V. Talapin, B. E. Cohen and P. J. Schuck, *Proc. Natl. Acad. Sci. U. S. A.*, 2009, **106**, 10917.
15 M. Haase, S. Heer, K. Kömpe and H. U. Güdel, *Adv. Mater.*, 2004, **16**, 2102.
16 N. J. J. Johnson, W. Oakden, G. J. Stanisz, R. S. Prosser and F. C. J. M. van Veggel, *Chem. Mater.*, 2011, **23**, 3714.
17 Q. Liu, Y. Sun, T. Yang, W. Feng, C. Li and F. Li, *J. Am. Chem. Soc.*, 2011, **133**, 17122.
18 F. Wang, J. Wang, J. Xu, X. Xue, H. Chen and X. Liu, *Spectrosc. Lett.*, 2010, **43**, 400.
19 E. van der Kolk, P. Dorenbos, K. Kramer, D. Biner and H. U. Gudel, *Phys. Rev. B: Condens. Matter Mater. Phys.*, 2008, **77**, 125110.
20 G. Chen, J. Shen, T. Y. Ohulchanskyy, N. J. Patel, A. Kutikov, Z. Li, J. Song, R. K. Pandey, H. Agren, P. N. Prasad and G. Han, *ACS Nano*, 2012, **6**, 8280.
21 H.-X. Mai, Y.-W. Zhang, R. Si, Z.-G. Yan, L.-D. Sun, L.-P. You and C.-H. Yan, *J. Am. Chem. Soc.*, 2006, **128**, 6426.
22 L. W. Yang, Y. Li, Y. C. Li, J. J. Li, J. H. Hao, J. X. Zhong and P. K. Chu, *J. Mater. Chem.*, 2012, **22**, 2254.
23 Q. Cheng, J. Sui and W. Cai, *Nanoscale*, 2012, **4**, 779.
24 G. Chen, T. Y. Ohulchanskyy, W. C. Law, H. Agren and P. N. Prasad, *Nanoscale*, 2011, **3**, 2003.
25 R. Naccache, F. Vetrone, V. Mahalingam, L. A. Cuccia and J. A. Capobianco, *Chem. Mater.*, 2009, **21**, 717.
26 K. W. Krämer, D. Biner, G. Frei, H. U. Güdel, M. P. Hehlen and S. R. Lüthi, *Chem. Mater.*, 2004, **16**, 1244.
27 R. T. Wegh, H. Donker, K. D. Oskam and A. Meijerink, *Science*, 1999, **283**, 663.
28 V. Mahalingam, F. Vetrone, R. Naccache, A. Speghini and J. A. Capobianco, *Adv. Mater.*, 2009, **21**, 4025.
29 J. Wang, F. Wang, J. Xu, Y. Wang, Y. Liu, X. Chen, H. Chen and X. Liu, *C. R. Chim.*, 2010, **13**, 731.
30 G. Chen, T. Y. Ohulchanskyy, A. Kachynski, H. Agren and P. N. Prasad, *ACS Nano*, 2011, **5**, 4981.
31 V. Mahalingam, R. Naccache, F. Vetrone and J. A. Capobianco, *Chem.–Eur. J.*, 2009, **15**, 9660.
32 Y.-P. Du, Y.-W. Zhang, L.-D. Sun and C.-H. Yan, *Dalton Trans.*, 2009, 8574.
33 F. Wang, Y. Han, C. S. Lim, Y. Lu, J. Wang, J. Xu, H. Chen, C. Zhang, M. Hong and X. Liu, *Nature*, 2010, **463**, 1061.
34 F. Wang, J. Wang and X. Liu, *Angew. Chem., Int. Ed.*, 2010, **49**, 7456.
35 Q. Su, S. Han, X. Xie, H. Zhu, H. Chen, C.-K. Chen, R.-S. Liu, X. Chen, F. Wang and X. Liu, *J. Am. Chem. Soc.*, 2012, **134**, 20849.
36 C. Dong, J. Pichaandi, T. Regier and F. C. J. M. van Veggel, *J. Phys. Chem. C*, 2011, **115**, 15950.
37 J. Park, K. J. An, Y. Hwang, J.-G. Park, H.-J. Noh, J.-Y. Kim, J.-H. Park, N.-M. Hwang and T. Hyeon, *Nat. Mater.*, 2004, **3**, 891.
38 G. Kresse and J. Furthmüller, *Phys. Rev. B: Condens. Matter Mater. Phys.*, 1996, **54**, 11169.
39 J. P. Perdew, A. Ruzsinszky, G. I. Csonka, O. A. Vydrov, G. E. Scuseria, L. A. Constantin, X. Zhou and K. Burke, *Phys. Rev. Lett.*, 2008, **100**, 136406.
40 P. E. Blöchl, *Phys. Rev. B: Condens. Matter Mater. Phys.*, 1994, **50**, 17953.
41 J.-C. Boyer and F. C. J. M. van Veggel, *Nanoscale*, 2010, **2**, 1417.
42 H. X. Mai, Y. W. Zhang, L. D. Sun and C. H. Yan, *J. Phys. Chem. C*, 2007, **111**, 13721.
43 X. Ye, J. E. Collins, Y. Kang, J. Chen, D. T. N. Chen, A. G. Yodh and C. B. Murray, *Proc. Natl. Acad. Sci. U. S. A.*, 2010, **107**, 22430.
44 H. Wang and T. Nann, *Nanoscale Res. Lett.*, 2011, **6**, 267.
45 G. Henkelman, A. Arnaldsson and H. Jónsson, *Comput. Mater. Sci.*, 2006, **36**, 354.
46 W. Tang, E. Sanville and G. Henkelman, *J. Phys.: Condens. Matter*, 2009, **21**, 084204.
47 R. E. Thoma, G. D. Brunton, R. A. Penneman and T. K. Keenan, *Inorg. Chem.*, 1970, **9**, 1096.
48 A. V. Goryunov, A. I. Popov, N. M. Khajdukov and P. P. Fedorov, *Mater. Res. Bull.*, 1992, **27**, 213.